01 Sep 2012

A Method to Generate Pressure Gradients for Molecular Simulation of Pressure-Driven Flows in Nanochannels

Zhi Liang
Missouri University of Science and Technology, zlch5@mst.edu

Hai-Lung Tsai
Missouri University of Science and Technology, tsai@mst.edu

Recommended Citation

Z. Liang and H. Tsai, "A Method to Generate Pressure Gradients for Molecular Simulation of Pressure-Driven Flows in Nanochannels," *Microfluidics and Nanofluidics*, vol. 13, no. 2, pp. 289 - 298, Springer, Sep 2012.
The definitive version is available at https://doi.org/10.1007/s10404-012-0960-4

Microfluid Nanofluid (2012) 13:289–298
DOI 10.1007/s10404-012-0960-4

RESEARCH PAPER

A method to generate pressure gradients for molecular simulation of pressure-driven flows in nanochannels

Zhi Liang · Hai-Lung Tsai

Received: 1 January 2012 / Accepted: 22 February 2012 / Published online: 4 March 2012

Abstract One of the difficulties in molecular simulation of pressure-driven fluid flow in nanochannels is to find an appropriate pressure control method. When periodic boundary conditions (PBCs) are applied, a gravity-like field has been widely used to replace actual pressure gradients. The gravity-fed method is not only artificial, but not adequate for studying properties of fluid systems which are essentially inhomogeneous in the flow direction. In this paper, a method is proposed which can generate any desired pressure difference to drive the fluid flow by attaching a "pump" to the nanofluidic system, while the model is still compatible with PBCs. The molecular dynamics model based on the proposed method is applied to incompressible flows in smooth nanochannels, and the predicted velocity profiles are identical to those by the gravity-fed method, as expected. For compressible flows, the proposed model successfully predicts the changes of fluid density and velocity profile in the flow direction, while the gravity-fed method can only predict constant fluid properties. For fluid flows in nanochannels with a variable cross-sectional area, the proposed model predicts higher mass flow rates as compared to the gravity-fed method and possible reasons for the difference are discussed.

Keywords Molecular dynamics · Pressure-driven flow · Nanochannel · Pressure gradient · Compressible flow · Variable cross-sectional area

Z. Liang · H.-L. Tsai (✉)
Department of Mechanical and Aerospace Engineering,
Missouri University of Science and Technology,
400 W. 13th Street, Rolla, MO 65409, USA
e-mail: tsai@mst.edu

1 Introduction

Fluid flow through nanoporous materials has attracted great attention in recent years because of its potential applications in molecular detection, gas storage, membrane separation and energy conversion devices (Ajayan et al. 1995; Liu et al. 1999; Zheng et al. 2003; van der Heyden et al. 2005, 2007). Due to the high surface-to-volume ratio, the molecular scale boundary characteristics, which are determined by the fluid–solid interaction, are important in understanding the behavior of nanoscale fluid flows (Cieplak et al. 2006). In many cases (Liu and Li 2009; Takaba et al. 2007; Huang et al. 2007), the fluid flux in a nanofluidic system deviates greatly from that predicted by the continuum theory, and the Navier–Stokes equations lose their validity. Therefore, molecular dynamics (MD) simulations which are ideally suited to nanosized systems have been widely used to investigate the nanoscale fluid flow.

One of the difficulties in MD simulations of the pressure-driven fluid flow in a nanochannel is to find an appropriate pressure control method. Although traditional pressure control methods such as those developed by Andersen (1980) and Berendsen et al. (1984) are widely used in equilibrium MD simulations, these methods are difficult to be applied in non-equilibrium MD simulations of pressure-driven flows in which there is a pressure-gradient in the flow direction (Takaba et al. 2007). The most widely used method to resolve this problem is called gravity-fed method in which an external gravity-like field is uniformly applied to the fluidic system, and the particles are driven by this field (Alexiadis and Kassinos 2008). The advantages of this method are its simplicity and low-computational costs. In the gravity-fed method, due to the periodic boundary conditions (PBCs) applied in the flow direction, the fluid properties, such as density, at the inlet

and outlet of the fluid flow are forced to be identical. In many cases, fluid property variation in the flow direction is negligible and, hence, the actual pressure gradient can be replaced by an artificial external field. However, for compressible fluids, such as gases and supercritical fluids, a small change in pressure may result in large changes in, for example, density. The application of transport of gases in nanochannels includes precise delivery of gases, separating gases, etc., using carbon nanotubes and zeolites (Wang et al. 1999). With the increase of computational capability, molecular simulation can be used to study a system with millions of atoms, which corresponds to a nanochannel with the length of hundreds of nanometer or even several micrometers. In this case, the density variation over the length of channel is non-negligible, and the gravity-fed method loses its validity. Therefore, the major issue of the gravity-fed method is that the method is not suitable for nanoscale fluid flows whose properties vary in the flow direction (Hanasaki and Nakatani 2006). Furthermore, replacing an actual pressure gradient with a gravity-like field in a two- or three-dimensional flow, such as the flow in a nanochannel with variable cross-sectional areas, may also be problematic. Hence, it is necessary to develop an efficient method to generate an actual pressure gradient for molecular simulation of pressure-driven flows in nanochannels.

To drive a fluid flow with an actual pressure gradient, several other methods have been proposed. Heffelfinger and van Swol (1994) developed a dual control volume grand canonical molecular dynamics (DCV-GCMD) method. In the DCV-GCMD method, to produce a chemical potential (or pressure) gradient, a certain number of grand canonical Monte Carlo steps are conducted to insert or delete particles in the two control volumes located at each end of the system. The disadvantage of the DCV-GCMD method is that the computational cost becomes prohibitive if it is used to investigate dense fluid systems or polyatomic molecular systems (Alexiadis and Kassinos 2008). Therefore, the use of the DCV-GCMD method is limited to low density and simple fluidic systems. Takaba et al. (2007) developed a pressure control method by using two fluctuating walls. The two walls behave as a frictionless piston and push the liquid in the high pressure source region across a nanopore into a low pressure permeate region. Using two fluctuating walls, a constant pressure difference between the inlet and outlet of the nanopore can be maintained in the simulation. The drawback of this method is that the majority of fluid particles in the simulation system is in the source or permeate region, while fluid particles in the pore region which are actually used for the calculation of transport properties of the fluid flow in nanopores only account for a small portion. Moreover, the maximum simulation length is limited by the total number of fluid particles in the source region. Once all fluid particles in the source region flow to the permeate region, the simulation has to stop. Another approach, called fluidized piston model, was proposed by Hanasaki and Nakatani (2006). In this model, a fluidized piston region which includes a particle insertion volume and a fluidized piston is located at the upstream of the fluid flow and presses the rest of fluid in the system. PBCs cannot be used with this approach since Hanasaki and Nakatani found that unrealistic interactions can arise when the downstream end is directly connected to the upstream end. Although this method also produces actual pressure gradients, the algorithm provided by Hanasaki and Nakatani seems much more complicated than that of the widely used gravity-fed method. Hence, the fluctuating wall method and the fluidized piston method are not widely used due to the relatively high-computational cost or their complexity.

In this work, we propose a method that can generate desired pressure gradients, and the MD model based on the proposed method can be used to simulate both compressible and incompressible nanoscale pressure-driven fluid flows. The method is easy to be implemented and the computational cost is comparable to that of the widely used gravity-fed method. The proposed model is applied to fluid flows in planar nanochannels with different surface wettabilities. In addition, fluid flows in a nanochannel with sudden expansion (two-dimensional flows) are also investigated. The simulation results from the proposed model are compared to those from the gravity-fed method to show the advantages of the proposed model.

2 MD model

2.1 Generation of a desired pressure difference

To explain the principle of the proposed model, we show in Fig. 1 a typical nanofluidic system which is used to simulate a pressure-driven fluid flow in a nanochannel bounded by two solid walls. As depicted in Fig. 1, the simulation system contains two regions: one is the pressure-driven flow region and the other is the "pump" region that generates a constant pressure difference to drive the fluid flow. PBCs are applied in the x- and y-directions. In the pressure-driven flow region, the pressure of fluid gradually decreases in the flow direction due to the friction of the solid walls. In the pump region, the pressure increases in the flow direction by applying an external pump force f_{pump}. To find the appropriate f_{pump} for generating the desired pressure difference, a control volume analysis is applied to the volume of fluid in the pump region. As shown in Fig. 1, the forces acting on the fluid in the pump region include f_{pump}, the pump force, f_{w}, the force exerted by solid walls, and $f_{\text{p}} = (P_{\text{in}} - P_{\text{out}})A$, the pressure force, where

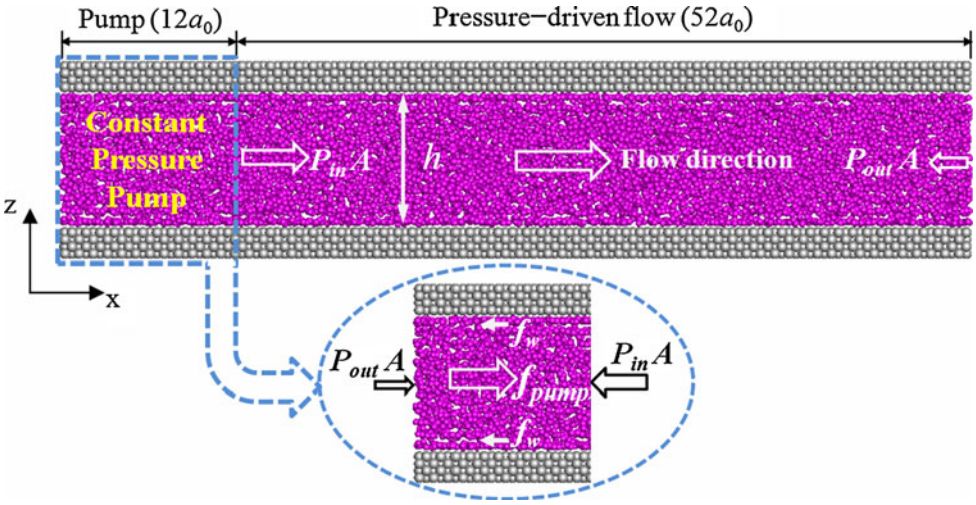

Fig. 1 Schematic diagram of the proposed method. The system contains parallel Ag walls and a fluid Ar thin film. The Ar thin film is equilibrated at $T = 100$ K and $\rho = 34.22$ mol/L with $\varepsilon_{Ag-Ar} = 60$ K. PBCs are applied in the x- and y-directions

P_{in} and P_{out} denote, respectively, the inlet and outlet pressure of the pressure-driven flow. Applying the linear momentum equation to the pump region, the following equation is obtained at the steady state:

$$f_{pump} - f_w - f_p = \left[\int \rho v_x^2 dA\right]_{out} - \left[\int \rho v_x^2 dA\right]_{in} \quad (1)$$

where the subscripts 'out' and 'in' represent, respectively, the outlet and inlet of the pump. Due to the PBC applied in the x-direction, the outlet of the pump is actually the inlet of the pressure-driven flow, and the inlet of the pump is the outlet of the pressure-driven flow. In Eq. 1, ρ and v_x represent the local average density and the x-component of local average stream velocity at the inlet or outlet of the pump region, and A represents the cross-section area. If the fluid properties are homogeneous in the flow direction, the two terms on the right side of Eq. 1 cancel each other. In this case, the pump force f_{pump} is simply

$$f_{pump} = f_w + f_p \quad (2)$$

At the steady state, the average pressure force $f_p = (P_{in} - P_{out})A$ is determined by $(P_{in} - P_{out})$ which is equal to the preset desired pressure difference. In the simulation, therefore, we only need to calculate f_w, the x-component of force exerted by solid walls on fluid molecules within the pump region at each time step and find the corresponding f_{pump} according to Eq. 2. Each f_w and f_{pump} fluctuates around a constant value at the steady state. Similar to the MD work on Poiseuille flow by Nagayama and Cheng (2004), f_{pump} is applied uniformly to fluid particles in the pump region in the simulation. After an initial acceleration period, the pump can generate a constant preset pressure difference using the aforementioned method.

If the fluid density varies in the flow direction, the two terms on the right side of Eq. 1 do not cancel each other and, hence, they need to be taken into account as Eq. 3.

$$f_{pump} = f_w + f_p + \left(\left[\int \rho v_x^2 dA\right]_{out} - \left[\int \rho v_x^2 dA\right]_{in}\right) \quad (3)$$

In this case, the local density and velocity of fluid at the outlet and inlet of the pump region should also be calculated at each time step to determine the appropriate f_{pump} for the generation of the desired pressure difference. In nanochannel flows, the measured stream velocities by experiments (Holt et al. 2006; Kuang and Wang 2010) are generally less than 1 m/s. For such low flow rates, the last two terms in Eq. 3 can be neglected. In most cases, only when the fluid flow has a high stream velocity ($\sim$100 m/s) and there is a considerable variation ($\sim$100 kg/m^3) in fluid density, the last two terms in Eq. 3 become important. Moreover, the calculation of the last two terms in Eq. 3 is subjected to a relatively large uncertainty. In the simulation, therefore, these two terms are not considered in the initial acceleration period. However, after the fluidic system reaches an intermediate steady state, the last two terms in Eq. 3 are taken into account to let the system reach the final steady state and generate the desired pressure difference.

2.2 Simulation systems

To show the validity of the proposed model, the simulation method is applied to a nanofluidic system which consists of two parallel Ag walls which sandwich a thin film of fluid Ar, as shown in Fig. 1. Each of the Ag walls is described as a [1 0 0]-oriented perfect fcc crystal of lengths $64a_0$ in the x-direction, $12a_0$ in the y-direction and $2a_0$ in the z-direction, where $a_0 = 4.086$ Å is the lattice constant of Ag (Lincoln et al. 1967). The channel width h is set to 4 or 6 nm in different simulation cases. The Ag–Ag interaction is modeled by the Morse potential with parameters $r_e = 3.13$ Å, $a = 1.3535$ Å^{-1} and $D = 3{,}775$ K (Lincoln

et al. 1967). The Ar–Ar interaction is modeled by the Lennard-Jones (LJ) 12–6 potential with parameters $\sigma = 3.41$ Å and $\varepsilon = 119.8$ K (Maitland et al. 1981). The LJ potential is also used to simulate the interactions between Ar and Ag. The parameters $\sigma_{Ag-Ar} = 3.12$ Å and $\varepsilon_{Ag-Ar} = 204$ K, which corresponds to a wetting condition (Yang 2006), are chosen so that the Ag–Ar potential reproduces the experimental data of adsorption height and energy for the Ar/Ag system (Unguris et al. 1981). As the value of solid–fluid binding energy ε_{Ag-Ar} represents the degree of surface wettability, the effect of surface wettability can be studied by varying ε_{Ag-Ar} from 204 K (wetting condition) to 60 or 12 K (less-wetting condition). Such a variation of wetting properties can be accomplished experimentally by coating surfaces with different kinds of molecules (Auletta et al. 2004). The cut-off radius for all interactions is 2.5σ. As depicted in Fig. 1, we set the first $12a_0$-long segment of the fluidic system as the pump region, and the remaining $52a_0$-long segment as the pressure-driven flow region. Note that the length of pump region should not be too small, because the fluid velocity at the inlet of the pressure-driven flow should not be strongly correlated with that at the outlet. On the other hand, if the pump region is too long, the computational cost becomes higher. To make a compromise, we found that a $12a_0$-long pump region is appropriate. All fluid flows considered in this work are driven by a constant pressure difference of 5 MPa. Hence, the pressure force, f_p, in Eqs. 2 and 3 is fixed at 5(MPa) $\times$ $12a_0$ $\times$ h. The force exerted by solid walls in Eqs. 2 and 3 is calculated at each time step by $f_w = -\sum_i^{\text{fluid}} \sum_j^{\text{wall}} f_{ij,x}$ where the first summation is over all fluid molecules in the pump region and the second summation is over all solid atoms. The subscript x indicates the force in the x direction.

To show the advantages of the proposed method, the fluid flows driven by the same pressure difference 5 MPa using the gravity-fed method are also investigated for comparison. When applying the gravity-fed method, the pump region is removed and only the $52a_0$-long pressure-driven flow region is used in the simulation. PBCs are still applied in the x- and y-directions. A driving force equal to f_p/N_{Ar}, where N_{Ar} is the total number of Ar atoms in the system, is applied to each Ar atom at each time step.

In all simulation cases, the whole nanofluidic system is first equilibrated at the desired temperature and density for 300 ps, and then the driving force is applied to the pump region (proposed method) or the pressure-driven flow region (gravity-fed method) for 20 ns to let the system reach a steady state. Finally, another 80 ns is used for data collection and averaging. To maintain a stable system, the Ag atoms in the outmost layers of each solid wall are fixed, while the Ag atoms in the other three layers of each wall are free to vibrate. Since thermostating a confined fluid during the non-equilibrium MD simulation may lead to significant unpredictable and unphysical material properties and underlying dynamics (Bernardi et al. 2010), a Nose–Hoover thermostat (Frenkel and Smit 2002) is applied to the wall atoms to maintain a desired temperature (Kannam et al. 2011). In the simulation, the equations of motion for vibrating wall atoms are coupled with two Nose–Hoover chains, while no thermostat is applied to the fluid. The viscous heat generated by the fluid is being taken away by the constant-temperature wall. All equations of motions are integrated by the velocity Verlet Scheme. At the steady state, the mass flow rate is determined by

$$\dot{m}_{MD} = \sum m_i v_{x,i} \Big/ L_x \tag{4}$$

where m_i represents the mass of fluid atom i, $v_{x,i}$ represents the velocity of atom i in the x-direction and L_x represents the length of the pressure-driven flow region. The summation in Eq. 4 is over all fluid atoms in the pressure-driven flow region.

3 Simulation results

3.1 Incompressible fluid flows

We first consider fluid Ar at $T = 100$ K and $\rho = 34.22$ mol/L so that Ar is at the liquid state. For liquid Ar close to such a state, a 5 MPa variation of pressure can only change the Ar density by <1%. Hence, the fluid flow in this case can be safely considered to be an incompressible flow and Eq. 2 is applied to generate a constant pressure difference. For an incompressible flow, whose density is constant in the flow direction, the velocity profile or the flow rate predicted by the proposed model should be identical to that predicted by the gravity-fed method. In the simulation, the channel width is set to 4 nm. The initial Ar structure is arranged with a [1 0 0]-oriented fcc lattice. The lattice constant is equal to 5.44 Å. The equilibrium Ar structures in the nanochannel are obtained by immersing a $72a_0$-long channel in a liquid Ar bath at $T = 100$ K and $\rho = 34.22$ mol/L. The equilibrated liquid Ar at the center $64a_0$-long segment is used for the later simulations of pressure-driven flows. A snapshot of equilibrated liquid Ar in the case of $\varepsilon_{Ag-Ar} = 60$ K is shown in Fig. 1. The time step size used in the simulation is 6 fs.

Each of the proposed method and the gravity-fed method is applied to the same fluid system. Two surface wettabilities are considered by setting ε_{Ag-Ar} to 204 and 60 K. To determine the velocity profile for each case, the liquid Ar is divided evenly into 12 layers in the z-direction, and the thickness of each layer is 3.33 Å which is

approximately equal to σ. Due to the long simulation time, the uncertainties of the calculated velocities are generally less than 2%. In Fig. 2, we show velocity profiles for $\varepsilon_{\text{Ag–Ar}} = 204$ K and for $\varepsilon_{\text{Ag–Ar}} = 60$ K. It is seen from Fig. 2 that the velocity profiles calculated from the proposed method and the gravity-fed method are almost identical, as expected. The parabolic profile predicted by the continuum theory is generally preserved in both the wetting and less-wetting cases. On the other hand, stronger solid–fluid interactions result in higher viscosity at the interface region (Nagayama and Cheng 2004). Hence, it is also found in Fig. 2 that the velocity profile, especially at the interface region, depends on surface wettability. An evidence of velocity slip at the less-wetting solid–liquid interface ($\varepsilon_{\text{Ag–Ar}} = 60$ K) is observed. The slip boundary condition found in our simulation is consistent with the findings in extensive literatures (Barrat and Bocquet 1999; Yang 2006; Li et al. 2010; Kannam et al. 2011).

In addition, we calculate the pressure and density distribution of fluid in the flow direction. In the calculation, the channel is divided evenly into 16 segments in the flow direction. The first 3 segments are in the pump region and the remaining 13 segments are in the pressure-driven flow region. The pressure of fluid in each segment is determined by $F_{\text{Ar}}/A_{\text{S}}$, where F_{Ar} is the total pressure force acting on the solid wall in the segment, and A_{S} is the surface area of the solid wall in the segment. In the simulation, F_{Ar} is determined by

$$F_{\text{Ar}} = \frac{1}{2}\left[\left(\sum_{i}^{\text{wall}}\sum_{j}^{\text{fluid}} f_{ij,z}\right)_{\text{top}} - \left(\sum_{i}^{\text{wall}}\sum_{j}^{\text{fluid}} f_{ij,z}\right)_{\text{bottom}}\right] \quad (5)$$

where the first summation in round brackets is over all solid atoms in the segment, the second summation is over all Ar atoms in the fluid, the subscript z indicates, the force in the z-direction, top and bottom represent top-solid wall and bottom-solid wall. Note if more segments are selected, a more accurate pressure distribution along the flow direction can be obtained. Figure 3 shows the pressure and density distribution in the case of $\varepsilon_{\text{Ag–Ar}} = 60$ K. The pressure-driven flow region starts at $x = 0$ and $x < 0$ is the pump region. The uncertainties of pressure and density are less than 1% and 0.2%, respectively. It is evident from Fig. 3 that the pressure increases in the pump region and decreases in the pressure-driven flow region, and the pressure difference between the inlet ($x = 0$) and the outlet ($x \approx 21.25$ nm) is approximately 5 MPa. The proposed method in fact has some similarity with the method used to generate temperature differences in a periodic system (Liang and Tsai 2011). A linear pressure drop is observed in Fig. 3, which proves that the fluid flow is driven by the actual pressure gradient. Due to the pressure variation, the fluid density is slightly changed in the flow direction. However, the maximum deviation from the average density is found only about 0.5%. Therefore, the inhomogeneity in the flow direction induced by pressure gradient is negligible. In the inset of Fig. 3, the pressure and density distributions obtained from the gravity-fed method are shown. It is seen that the pressure and density are constant in the flow direction. Note that the density of the confined liquid Ar, shown in Fig. 3, is slightly smaller than the density of Ar in the liquid bath. In the case of $\varepsilon_{\text{Ag–Ar}} = 60$ K, the

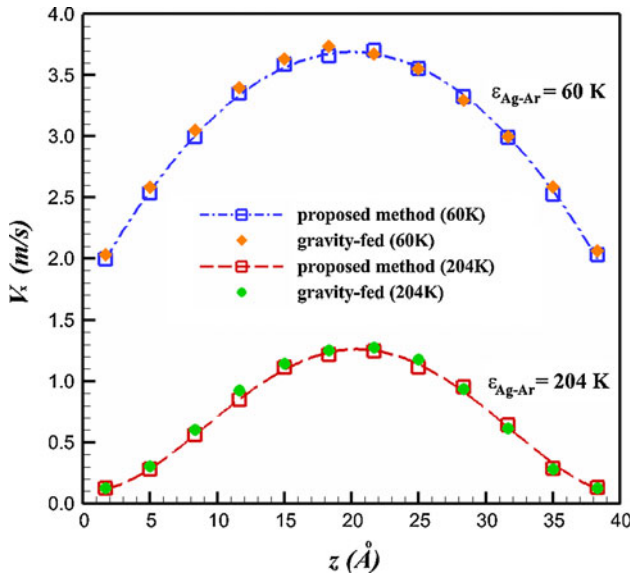

Fig. 2 Velocity profiles obtained from the proposed method and the gravity-fed method for liquid Ar flowing in a 4-nm wide planar channel. The uncertainty is less than the size of the symbol

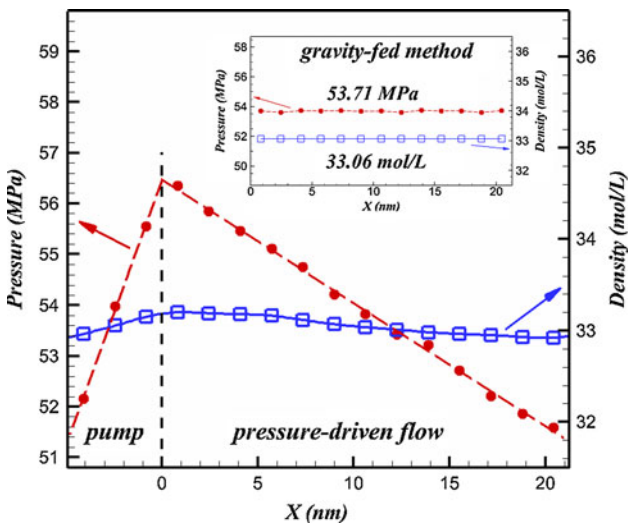

Fig. 3 Variations of pressure and density in the flow direction obtained from the proposed method and the gravity-fed method (*inset*) for liquid Ar flowing in a 4-nm wide planar channel with $\varepsilon_{\text{Ag–Ar}} = 60$ K. The uncertainty is less than the size of the symbol

solid–liquid binding energy is much smaller than the liquid–liquid binding energy. The smaller solid–liquid binding energy results in a relatively smaller Ar density at the region close to the solid–liquid interface and a relatively smaller average Ar density.

It is seen in Fig. 3 that the pressure at the inlet of the pressure-driven flow region is higher than the constant pressure in the gravity-driven flow, while the pressure at the outlet of the pressure-driven flow region is lower than the constant pressure in the gravity-driven flow. The result indicates that the "pump" attached to the pressure-driven flow has two effects. (1) The pump force pushes fluid atoms towards the inlet of the pressure-driven flow region, which increases the pressure at the inlet. (2) The pump force pulls fluid atoms away from the outlet of the pressure-driven flow region, which decreases the pressure at the outlet. Due to these two effects, a constant pressure difference is achieved at the steady state, while the average pressure of the pressure-driven flow is close to the constant pressure in the gravity-driven flow. To estimate the entrance (or exit) effect at the inlet (or outlet) of the pressure-driven flow, one can use the correlation $L_e/h \approx 0.06Re_h$ (Schlichting 1979) for laminar flow where L_e represents the entrance length. To evaluate the Reynolds number Re_h, we use $\rho = 1{,}367$ kg/m^3 (34.22 mol/L) for the fluid density, $u_0 = 3$ m/s for the entrance velocity, $h = 4$ nm for the channel height and $\mu = 2.26 \times 10^{-4}$ $Pa{\cdot}s$ for the viscosity of liquid Ar which is determined by employing an equilibrium MD simulation (Liang and Tsai 2010) on a bulk liquid Ar at $T = 100$ K and $\rho = 34.22$ mol/L. Accordingly, the entrance length $L_e \approx 0.0044h \approx 0.017$ nm is much smaller than the total length ($\approx$21 nm) of the channel. The real entrance length may be even smaller than the above estimated value, because the velocity profile in the pump region is close to that in the pressure-driven flow. Therefore, the entrance (or exit) effect can be ignored in the simulation.

Based on the above comparisons in Figs. 2 and 3, it is concluded that by applying an actual pressure gradient to a simple nanoscale fluid flow whose density is almost constant in the flow direction has almost the same effect as by applying a uniform external field. The total computational cost of the proposed model is only about 20% higher than that of the gravity-fed method.

3.2 Compressible fluid flows

We now consider fluid Ar at $T = 200$ K and $\rho = 12.50$ mol/L so that Ar is at the supercritical state. For fluid Ar near the supercritical state, a 5 MPa variation of pressure can cause a considerable change (>20%) in Ar density (Linstrom and Mallard 2011). Therefore, the density variation in the flow direction cannot be neglected and Eq. 3 is applied to generate the desired pressure difference. The channel width is fixed at 4 nm and ε_{Ag-Ar} is set to 60 K. A similar method as described in the last section is used to determine the equilibrium Ar structure in the nanochannel at the desired temperature and density. The time step size used in the simulation is 4 fs.

As discussed before, the last two terms in Eq. 3 are not taken into account in the initial acceleration period. After 15 ns, the system reaches an intermediate steady state, and the last two terms in Eq. 3 are then included for 5 ns to let the system reach the final steady state. To calculate the local density and stream velocity at the outlet and inlet of the pump region, Ar atoms which are less than $2a_0$ away from the inlet or outlet of the pump region are used for data collection. The local density and velocity used in the calculation at each time step are always averaged from the data in the previous 500 ps period. Figure 4 shows the pressure and density variation of the supercritical Ar in the flow direction at the final steady state. It is seen that the pressure distribution is similar to that in the aforementioned liquid Ar flow. An almost linear pressure drop in the pressure-driven flow region is found. The pressure difference is equal to the desired value of 5 MPa. On the other hand, the decrease of density in the flow direction is not linear, which indicates that the density of confined fluids at the given supercritical state is not a linear function of pressure. An over 19% variation in fluid density is found in the flow direction. As shown in the inset of Fig. 4, such a variation of density is not seen in the gravity-fed method. According to the conservation of mass, the decrease of fluid density in the flow direction will result in the increase of velocity in the flow direction. Therefore, we divide the $52a_0$-long pressure-driven flow region evenly into four

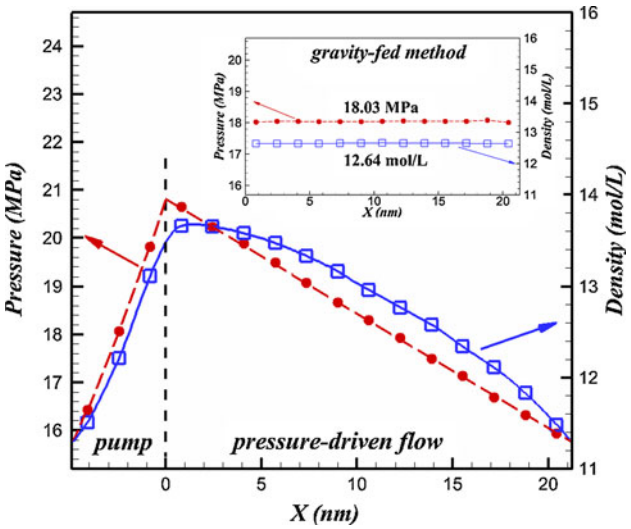

Fig. 4 Variations of pressure and density in the flow direction obtained from the proposed method and the gravity-fed method (*inset*) for supercritical Ar flowing in a 4-nm wide planar channel with $\varepsilon_{Ag-Ar} = 60$ K. The uncertainty is less than the size of the symbol

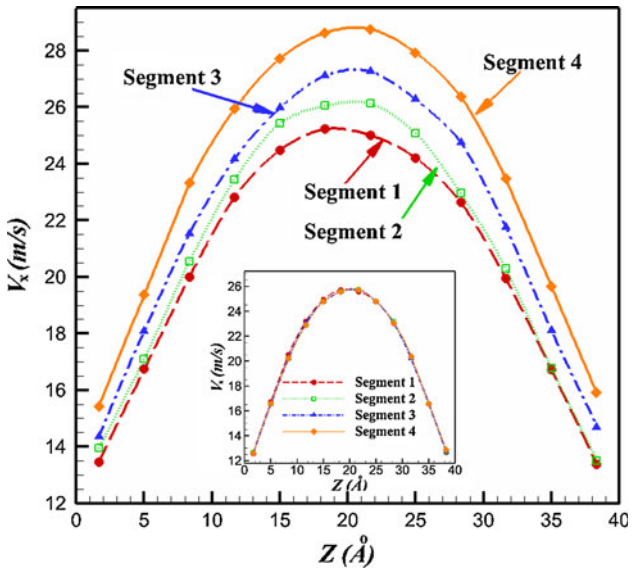

Fig. 5 Variations of velocity profile in the flow direction obtained from the proposed method and the gravity-fed method (*inset*) for supercritical Ar flowing in a 4-nm wide planar channel with $\varepsilon_{Ag-Ar} = 60$ K. The uncertainty is less than the size of the symbol

segments in the flow direction to see the expected velocity variation. It is shown in Fig. 5 that a Poiseuille type profile is obtained from the proposed model and gravity-fed method for supercritical fluid flows in each segment. The difference between these two methods is the velocity obtained from the proposed model, which gradually increases in the flow direction. Although the mass flow rate predicted by the gravity-fed method (3.39 ± 0.12 atoms/ps) is close to that predicted by the proposed model (3.31 ± 0.04 atoms/ps), the gravity-fed method fails to predict such an expected velocity variation in the flow direction. As shown in the inset of Fig. 5, the calculated velocity profiles in the four segments of the gravity-driven flow are all identical. From these comparisons, it is verified that when a fluid flow has a considerable change in density in the flow direction, it is inappropriate to replace an actual pressure gradient by a gravity-like field.

In fact, if the precise control of the pressure difference between the inlet and outlet is not required, one can simply use Eq. 2 in the simulation to generate a pressure difference which does not deviate too far from the desired value. In this case, the real pressure difference generated by the pump can be determined by an approach developed by Todd et al. (1995).

3.3 Nanochannels with variable cross-sectional area

Most nanochannels have a certain degree of surface roughness. The surface roughness may considerably change the cross-sectional area of a nanochannel in the flow direction. Experimental studies have shown that

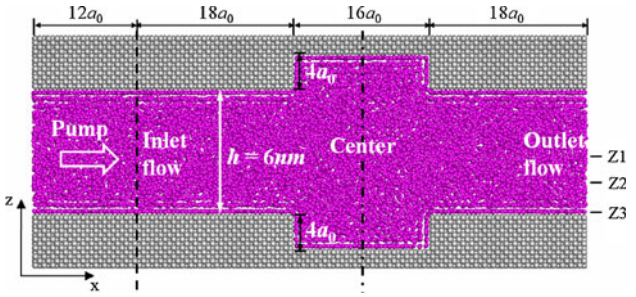

Fig. 6 A snapshot of liquid Ar flowing in a 6-nm wide channel with a $16a_0$-long, $4a_0$-deep sudden expansion in Ag solid walls and $\varepsilon_{Ag-Ar} = 204$ K. PBCs are applied in the x- and y-directions. z_1, z_2 and z_3 denote, respectively, the center of channel in the z-direction, the location 1.5 nm from z_1 and the location 0.5σ from the surface

surface roughness can significantly affect the transport properties of nanoscale fluid flows (Zhu and Granick 2002). We now consider liquid Ar at $T = 100$ K and $\rho = 34.22$ mol/L flowing in a nanochannel with sudden expansion in the flow direction. As shown in Fig. 6, the length of the pressure-driven flow region is still $52a_0$, and the length of the pump region is $12a_0$. In the center of the pressure-driven flow region, there is a $16a_0$-long, $4a_0$-deep sudden expansion between the two solid walls. The width of the channel at the inlet and outlet is 6 nm. Two surface wettabilities, $\varepsilon_{Ag-Ar} = 204$ K (wetting case) and $\varepsilon_{Ag-Ar} = 12$ K (less-wetting case), are considered. A similar method as described in the previous section is used to equilibrate Ar atoms in the nanochannel at the desired temperature and density. Equation (2) is then used to determine the appropriate pump force f_{pump} for the generation of the desired pressure difference 5 MPa. To verify if the desired pressure difference is really achieved, the x-component of the force acting on the solid walls by the Ar atoms in pressure-driven flow region is calculated. At the steady state, the calculated force should be equal to the pressure force 5 MPa $\times A$ where A is the inlet or outlet cross-sectional area. When the calculated force is divided by A, it is found that the value is equal to the preset pressure difference 5 MPa with the discrepancy <0.6% for the wetting and less-wetting cases. Hence, the proposed model is valid for investigating a pressure-driven flow in a nanochannel with variable cross-sectional area in the flow direction. A two-dimensional flow is expected in this case. The gravity-fed method replaces the actual pressure gradient with an artificial uniform external field. For two-dimensional flows, the validity of such a method is questionable.

At the steady state, the two-dimensional velocity distributions in the pressure-driven flow region for the wetting and less-wetting cases are shown in Fig. 7. The velocity averaging is done by employing rectangular prism bins with a size of 2σ in the x-direction, $12a_0$ in the y-direction

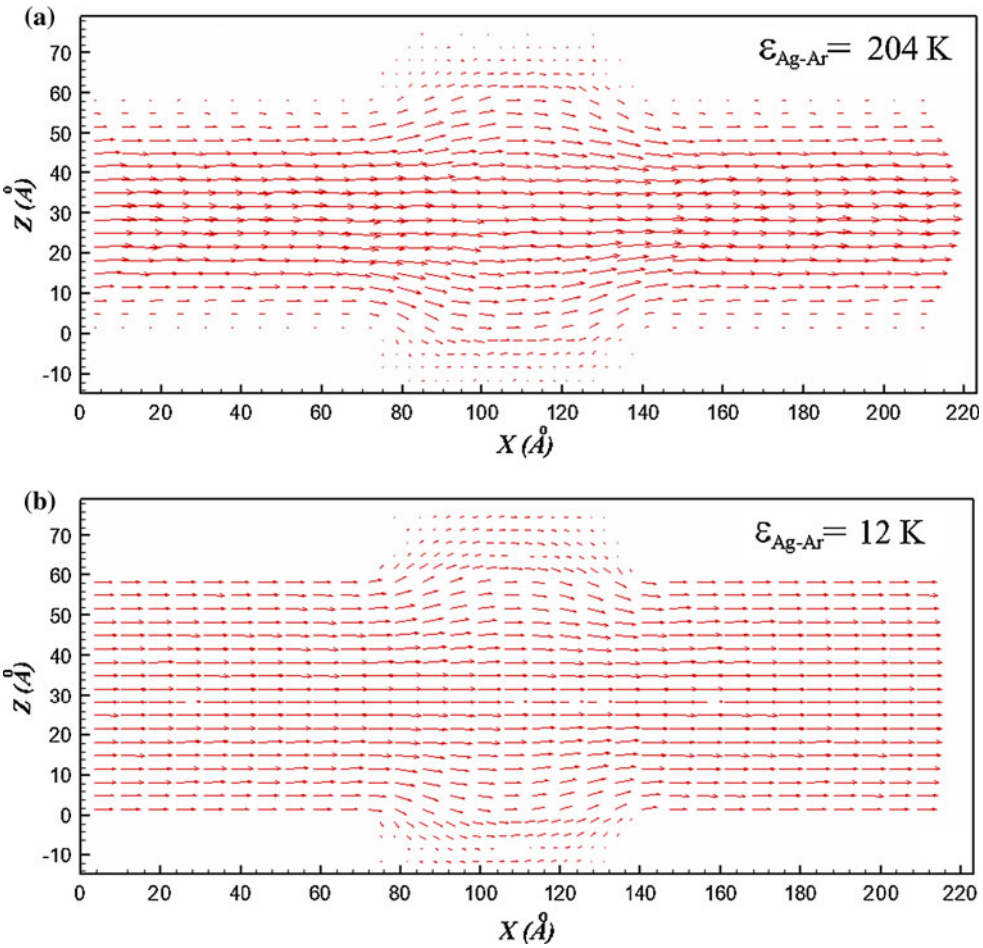

Fig. 7 Two-dimensional velocity distributions of liquid Ar flowing in a 6-nm wide channel with a sudden expansion in solid walls. **a** $\varepsilon_{Ag-Ar} = 204$ K (wetting); **b** $\varepsilon_{Ag-Ar} = 12$ K (less-wetting)

and σ in the z-direction. For both wetting and less-wetting cases, it is found that the velocity profile at the inlet of the pressure-driven flow region is identical to that at the outlet. Therefore, the last two terms in Eq. 3 do not need to be considered in the simulation. Variation of velocity profiles is only observed in the region close to the $16a_0$-long expansion region. Similar velocity distributions are also obtained by applying the gravity-fed method to the $52a_0$-long pressure-driven flow region. Figure 8 shows the variations of the x-component velocity in the flow direction and in the z-direction. The results from the gravity-fed method (scatters) are compared to those from the proposed model (lines) in Fig. 8. In Fig. 8a and c, the variations of velocity at three locations along the channel are shown, where z_1, z_2 and z_3 denote, respectively, the center of the channel in the z-direction, the location 1.5 nm from z_1 and the location 0.5σ from the surface as depicted in Fig. 6. Figure 8b and d show, respectively, the variations of velocity with z-coordinate at the center and at the inlet (or outlet) of the pressure-driven flow region.

Due to the strong attraction between Ag and Ar in the wetting case, the local stream velocity at the surface (z_3) is almost zero as shown in Fig. 8a. When the liquid Ar at z_3 flows into the expansion region, the Ar–Ar interaction, whose attraction strength is weaker, dominates the motion of Ar atoms. Accordingly, the liquid Ar at z_3 has a higher stream velocity in the expansion region. On the contrary, a large velocity slip at surfaces in the less-wetting case is found in Fig. 8c. Since the Ar–Ar attraction strength is much stronger than that of Ag–Ar in the less-wetting case, the liquid Ar at z_3 has a lower stream velocity in the expansion region. It is seen in Fig. 8c that the decelerating process has already started before the liquid Ar at z_3 enters the expansion region. According to the conservation of mass, therefore, the stream velocity at each of the locations z_1 and z_2 slightly increases before the liquid Ar enters the expansion region. At the center of the expansion region, as shown in Fig. 8a and c, the liquid Ar at each of z_1 and z_2 always has a lower stream velocity due to the increase of the cross-sectional area. From the aforementioned analysis one can see that the stream velocities in the expansion region are affected by the solid–liquid interaction relative to the liquid–liquid interaction. Although the strength of solid–liquid interaction also affects the density of fluid in

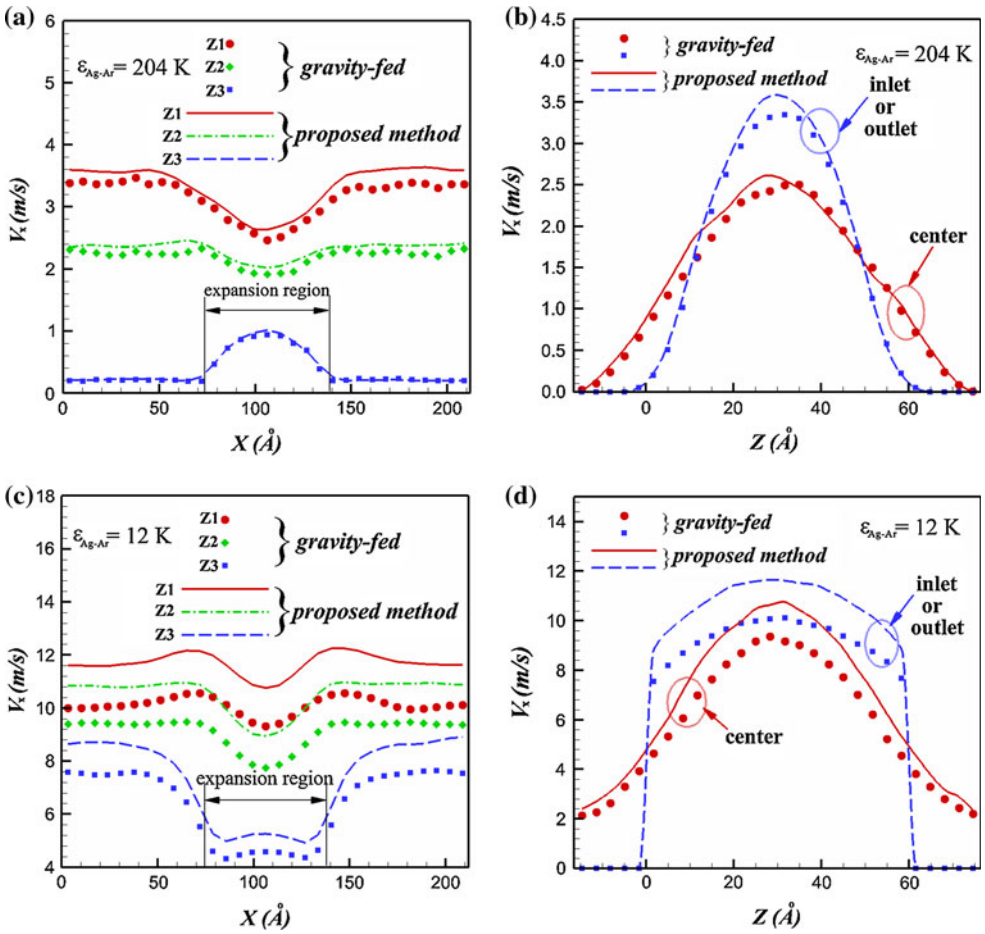

Fig. 8 Velocity distributions in the *x*-direction (**a** wetting and **c** less wetting) and in the *z*-direction (**b** wetting and **d** less wetting). Results from the proposed method are shown with *lines*, while *scatters* are for the gravity-fed method. The uncertainties of the calculated velocities are ±0.12 m/s in **a** and **b** and ±0.29 m/s in **c** and **d**

the interface region, the difference between the density of fluid in the interfacial region and the fluid density in the expansion region is less than 25% in the simulation. Therefore, the effect of density variation on the change of stream velocity in the flow direction is much smaller than the effect of solid–liquid interaction strength.

In the wetting case, it is seen in Fig. 8a and b that the velocity distribution calculated by the gravity-fed method is close to that by the proposed model. The only difference is that the velocity obtained from the gravity-fed method is slightly smaller than that from the proposed model. The mass flow rate predicted by the proposed model is 1.264 ± 0.023 atoms/ps, which is about 6.7% higher than 1.185 ± 0.028 atoms/ps predicted by the gravity-fed method. In the gravity-fed method, a constant external force f_p/N_{Ar}, where N_{Ar} is the total number of Ar atoms in the system, is applied to each Ar atom in the fluid. Some forces applied to the atoms at the edge of the expansion region are balanced by the force from the solid walls, especially the vertical walls. In this case, applying external forces with the same magnitude seems to be not reasonable. To further explain the problem in the gravity-fed method, we consider an extreme case where the pressure difference is the same, but the depth of the expansion region is much larger than $4a_0$. In this case, N_{Ar} becomes much larger and a large number of Ar atoms are located in the expansion region. The driving force applied on Ar atoms, deep in the expansion region, has a little effect on increasing the flow rate. Accordingly, the total external force which really has effects on driving the flow decreases. Therefore, it is reasonable to find that the gravity-fed method predicts a lower flow rate. Such a difference becomes more evident at the less-wetting case in which the flow rate is much greater. As shown in Fig. 8c and d, the gravity-fed method predicts lower velocities as compared to the proposed model. In the less-wetting case, the mass flow rate predicted by the proposed model is 6.223 ± 0.032 atoms/ps, which is about 15% higher than 5.417 ± 0.046 atoms/ps predicted by the gravity-fed method.

4 Conclusions

A method to generate a constant pressure difference between the inlet and outlet of the flow is achieved by attaching a constant pressure "pump" to the nanofluidic

system. An efficient MD model based on the proposed method has been developed for the molecular simulations of pressure-driven nanochannel flows. The simulation results explicitly show that the proposed model has advantages over the widely used gravity-fed method, which is not suitable for nanoscale fluid flows, whose properties vary along the flow direction. For pressure-driven fluid flows in a nanochannel with sudden expansion, the simulation results indicate that the proposed model predicts a higher mass flow rate as compared to the gravity-fed method. The proposed method is easy to be implemented, and the computational cost is comparable to that of the gravity-fed method. The current model can be readily extended to more complex nanofluidic systems, such as water flow in carbon nanotubes which comprises polyatomic molecules of practical interest.

Acknowledgments We thank National Institute for Computational Science (NICS) and National Center for Supercomputing Applications (NCSA) for providing us supercomputer resources for MD simulations.

References

Ajayan PM, Stephan O, Redlich Ph, Colliex C (1995) Carbon nanotubes as removable templates for metal oxide nanocomposites and nanostructures. Nature (London) 375:564–567

Alexiadis A, Kassinos S (2008) Molecular simulation of water in carbon nanotubes. Chem Rev 108:5014–5034

Andersen HC (1980) Molecular dynamics simulations at constant pressure and/or temperature. J Chem Phys 72:2384–2393

Auletta T, Dordi B, Mulder A, Sartori A, Onclin S, Bruinink CM, Peter M, Nijhuis A, Beijleveld H, Schonherr H, Vancso GJ, Casnati A, Ungaro R, Ravoo BJ, Huskens J, Reinhoudt DN (2004) Writing patterns of molecules on molecular printboards. Angew Chem Int Ed 43:369–373

Barrat JL, Bocquet L (1999) Large slip effect at a nonwetting fluid–solid interface. Phys Rev Lett 82:4671–4674

Berendsen HJC, Postma JPM, van Gunsteren WF, Di Nola A, Haak JR (1984) Molecular dynamics with coupling to an external bath. J Chem Phys 81:3684–3690

Bernardi S, Todd BD, Searles DJ (2010) Thermostating highly confined fluids. J Chem Phys 132:244706

Cieplak M, Koplik J, Banavar JR (2006) Nanoscale fluid flows in the vicinity of patterned surfaces. Phys Rev Lett 96:114502

Frenkel D, Smit B (2002) Understanding molecular simulation from algorithms to applications. Academic press, San Diego

Hanasaki I, Nakatani A (2006) Fluidized piston model for molecular dynamics simulations of hydrodynamic flow. Model Simul Mater Sci Eng 14:S9–S20

Heffelfinger GS, van Swol F (1994) Diffusion in Lennard–Jones fluids using dual control volume grand canonical molecular dynamics simulation (DCV–GCMD). J Chem Phys 100:7548–7552

Holt JK, Park HG, Wang YM, Stadermann M, Artyukhin AB, Grigoropoulos CP, Noy A, Bakajin O (2006) Fast mass transport through sub—2-nanometer carbon nanotubes. Science 312:1034–1037

Huang C, Choi PYK, Nandakumar K, Kostiuk LW (2007) Comparative study between continuum and atomistic approaches of liquid flow through a finite length cylindrical nanopore. J Chem Phys 126:224702

Kannam SK, Todd BD, Hansen JS, Daivis P (2011) Slip flow in graphene nanochannels. J Chem Phys 135:144701

Kuang C, Wang G (2010) A novel far–field nanoscopic velocimetry for nanofluidics. Lab Chip 10:240–245

Li Y, Xu J, Li D (2010) Molecular dynamics simulation of nanoscale liquid flows. Microfluid Nanofluid 9:1011–1031

Liang Z, Tsai HL (2010) Prediction of transport properties of a polyatomic gas. Fluid Phase Equilib 293:196–204

Liang Z, Tsai HL (2011) Effects of molecular film thickness on thermal conduction across solid-film interfaces. Phys Rev E 83:061603

Lincoln RC, Koliwad KM, Ghate PB (1967) Morse-potential evaluation of second- and third-order elastic constants of some cubic metals. Phys Rev 157:463–466

Linstrom PJ, Mallard WG (2011) National Institute of Standards and Technology, Gaithersburg MD, 20899. http://webbook.nist.gov

Liu C, Li ZG (2009) Flow regimes and parameter dependence in nanochannel flows. Phys Rev E 80:036302

Liu C, Fan Y, Cong HT, Cheng HM, Dreselhaus MS (1999) Hydrogen storage in single-walled carbon nanotubes at room temperature. Science 286:1127–1129

Maitland GC, Rigby M, Smith EB, Wakeham WA (1981) Intermolecular forces: their origin and determination. Clarendon Press, Oxford

Nagayama G, Cheng P (2004) Effects of interface wettability on microscale flow by molecular dynamics simulation. Int J Heat Mass Transf 47:501–513

Schlichting H (1979) Boundary layer theory, 7th edn. McGraw-Hill, New York

Takaba H, Onumata Y, Nakao S (2007) Molecular simulation of pressure-driven fluid flow in nanoporous membranes. J Chem Phys 127:054703

Todd BD, Evans DJ, Daivis PJ (1995) Pressure tensor for inhomogeneous fluids. Phys Rev E 52:1627–1638

Unguris J, Bruch LW, Moog ER, Webb MB (1981) Ar and Kr adsorption on Ag(111). Surf Sci 109:522–556

van der Heyden FHJ, Stein D, Dekker C (2005) Streaming current in a single nanofluidic channel. Phys Rev Lett 95:116104

van der Heyden FHJ, Bonthuis DJ, Stein D, Meyer C, Dekker C (2007) Power generation by pressure-driven transport of ions in nanofluidic channels. Nano Lett 7:1022–1025

Wang Q, Challa SR, Sholl DS, Jonhson JK (1999) Quantum sieving in carbon nanotubes and zerolites. Phys Rev Lett 82:956–959

Yang SC (2006) Effects of surface roughness and interface wettability on nanoscale flow in a nanochannel. Microfluid Nanofluid 2:501–511

Zheng M, Jagota A, Semke ED, Diner BA, Mclean RS, Lustig SR, Richardson RE, Tassi NG (2003) DNA-assisted dispersion and separation of carbon nanotubes. Nat Mater 2:338–342

Zhu Y, Granick S (2002) Limits of the hydrodynamic no-slip boundary condition. Phys Rev Lett 88:106102